

Wu, C.-Y., Nowacek, D. P., Nousek-McGregor, A. E., McGregor, R. and Howle, L. E. (2021) Computational fluid dynamics of flow regime and hydrodynamic forces generated by a gliding North Atlantic right whale (*Eubalaena glacialis*). *Marine Mammal Science*, 37(3), pp. 826-842.

There may be differences between this version and the published version. You are advised to consult the publisher's version if you wish to cite from it.

This is the peer reviewed version of the following article Balmer, P. and Stevenson, G. (2021) Relative stable categories and birationality. *Journal of the London Mathematical Society*, which has been published in final form at <https://doi.org/10.1111/mms.12798>. This article may be used for non-commercial purposes in accordance with [Wiley Terms and Conditions for Self-Archiving](#).

<http://eprints.gla.ac.uk/252337/>

Deposited on: 21 September 2021

Computational fluid dynamics of flow regime and hydrodynamic forces generated by a North Atlantic right whale (*Eubalaena glacialis*)

Chen-Yi Wu
Division of Marine Science and Conservation
Duke University Marine Laboratory
Beaufort, NC 28516, USA
chen.yi.wu@duke.edu

Laurens E. Howle, Ph.D. P.E.
Division of Marine Science and Conservation
Duke University Marine Laboratory
Beaufort, NC 28516, USA
and
Department of Mechanical Engineering and Material Science
Duke University
Durham, NC 27708, USA
and
Department of Radiology
Duke University Medical Center
Durham, NC 27705, USA

Anna E. Nousek-McGregor, Ph.D.
School of Life Sciences
University of Glasgow
Glasgow G12 8QQ, UK

Ross McGregor, Ph.D.
HiDef Aerial Surveying Ltd
Cleator Moor, Cumbria, CA25 5AU, UK

Douglas P. Nowacek, Ph.D.
Division of Marine Science and Conservation
Duke University Marine Laboratory
Beaufort, NC 28516, USA
and
Department of Electrical and Computer Engineering
Duke University
Durham, NC 27708, USA

Corresponding author: Laurens E. Howle, +1 919.660.5331, laurens.howle@duke.edu

Abstract

Accurate estimates of drag on marine animals are required to investigate the locomotive cost, propulsive efficiency, and the impacts of entanglement while the animal is carrying fishing gear. In this study, we performed computational fluid dynamics (CFD) analysis of a 10m (length over all, LoA) right whale to obtain baseline measurements of drag on the animal. Swimming speeds covering known right whale speed range (0.125 m/s to 8 m/s) were tested. We found a weak dependence between drag coefficient and Reynolds number. At a swimming speed of 2 m/s, we analyzed the boundary layer thicknesses, the flow regimes, and drag components. We found the thickest boundary layer at the lateral sides of the peduncle whereas the boundary layer thickness over the outer part of the flukes was less than 1.7cm. Laminar flow occurred over the anterior ~ 0.6 LoA and fully turbulent flow from ~ 0.8 LoA to the fluke notch. On the surfaces of the flukes outside of the body wake region, flow was laminar. Our most significant finding is that the drag coefficient (0.0071-0.0059) of a right whale, for swimming speeds ranging from 0.25 m/s to 2 m/s, is approximately twice that of many previous drag coefficient estimates for cetaceans.

Keywords: Right whale, *Eubalaena glacialis*, Hydrodynamics, Drag, CFD, boundary layer

Introduction

Drag occurs when an object moves through a fluid due to the viscosity of the fluid, which is the resistant force against the movement (Vogel 1994). The strength of drag is determined by physical properties such as fluid density, cross-section or wetted area of the object, and how fast it moves. This rule applies to living organisms as well, since they must overcome drag to move forward (Vogel 1994). Therefore, under selective pressure, ancestors of aquatic animals evolved streamlined body shapes to increase their fitness in an aquatic environment (Fish 1993a, Vogel 1994, Woodward *et al.* 2006). To estimate the required energy output, one needs to measure the drag on these animals and, because the product of drag and velocity is power, the rate at which energy for propulsion is generated also requires an estimate of the drag (Vogel 1994). For that reason, the higher the drag, the more power, and therefore energy, is required by the animal to maintain a constant swimming speed.

The North Atlantic right whale, *Eubalaena glacialis* (hereafter NARW), population declined dramatically and nearly to extinction due to commercial whaling in the nineteenth and twentieth centuries (Kraus *et al.* 2005). Currently, the NARW is one of the most endangered cetaceans worldwide with approximately 411 individuals remaining (Pettis *et al.* 2018). With few exceptions, hunting NARWs became illegal in 1935 and these animals have been protected by the U.S. federal laws, the Marine Mammal Protection Act and Endangered Species Act, which were enacted in the 1970s. However, NARWs are still on the edge of extinction due to two major anthropogenic causes of mortality: vessel strike and entanglement in fishing gear (Kraus *et al.* 2005, Sharp *et al.* 2019).

While the implementation of regulations on vessel speed and rerouting of shipping lanes in NARW habitats effectively decreased the mortalities due to collisions between vessels and NARWs (van der Hoop *et al.* 2015), entanglement in fishing gear has become a central issue for the NARW population (Knowlton *et al.* 2016, Kraus *et al.* 2016). During entanglement events, these NARWs may end up having impaired physical

functions (e.g., inhibited feeding attempts, emaciation, increased energy demands, etc.) for several months or years and eventually die due to drowning, starvation, or serious injuries (Cassoff *et al.* 2011, Moore 2014, Knowlton *et al.* 2016, Moore *et al.* 2010, van der Hoop *et al.* 2017b, Sharp *et al.* 2019). Therefore, understanding the mechanisms and consequences of entanglement is crucial yet challenging, because *in situ* data collection is unlikely due to unpredictable location and timing of entanglements.

Although some entangled NARWs demonstrated behavioral differences from unencumbered individuals such as altered swimming patterns and diving depths (van der Hoop *et al.* 2017c, van der Hoop *et al.* 2014), little is known about how these animals are affected by gear attachment in terms of energetic costs. Knowing the energetic costs of NARWs is of interest because once the animal cannot intake a sufficient amount of food to replenish additional energy output while carrying fishing gear, it may not only metabolize its storage fat and become thinner and unhealthy but lose its ability to accomplish tasks other than survival (e.g., migration and reproduction) and ultimately affect the population (Williams & Maresh 2015). Therefore, estimating drag on NARWs is an essential approach to assess how energy demand has changed due to increased drag resulting from entanglement (Howle *et al.* 2018).

Several attempts have been made to estimate the drag on aquatic animals or thrust power generated by those animals, including conducting fluid mechanical experiments in laboratories (Drucker & Lauder 2002), analyzing data collected by biologging tags in the field and from videotape recordings of captive animals (Fish 1993b, Fish 1998, Goldbogen *et al.* 2007, van der Hoop *et al.* 2017c), and calculating drag with computational models (Nousek-McGregor 2010, Shorter *et al.* 2014, Zhang *et al.* 2019).

With respect to the baseline drag estimates, computational fluid dynamics (CFD) models could be a solution when one tries to examine fluid mechanics of a fully-submerged marine animal (Shorter *et al.* 2014). Nousek-McGregor (2010) estimated drag on a NARW swimming at 0.514 m/s through a CFD model. Though accurate estimates of drag on marine animals are required if one wants to investigate the overall

locomotive cost (Nousek-McGregor 2010), the propulsive efficiency (van der Hoop et al. 2017c), and the impacts of entanglement with respect to energy expenditure while the animal is carrying fishing gear (van der Hoop et al. 2017b, van der Hoop *et al.* 2017a), to our knowledge no studies have systematically estimated hydrodynamic drag across the range of NARW's swimming speeds or analyzed flow regime on a gliding NARW.

Given the difficulties in measuring the drag on large whales in the field, we aimed to estimate the hydrodynamic forces using computer simulations. This study was designed to investigate the following questions: how does the flow regime and boundary layer thickness change along the longitudinal axis of the NARW? How do various hydrodynamic forces, such as shear stress, drag, and pressure disperse on the NARW? The methodological approach taken in this study is a CFD analysis over a morphologically accurate 10 m NARW model using a commercial flow solver (SolidWorks Flow Simulation 2019) to obtain baseline measurements of drag and other hydrodynamic parameters on the NARW model. The research presented here provides one of the first investigations into the hydrodynamic properties of free-swimming, un-entangled NARWs and the only one to our knowledge that tests the range of swimming speeds observed for NARWs.

Materials and Methods

In this study, CFD analysis was selected for providing detailed measurements of drag and other hydrodynamic parameters on a three-dimensional NARW model. Swimming speeds covering the known right whale range were tested. Using the CFD simulations, we analyzed (1) boundary layer thicknesses, (2) flow regimes, (3) shear stress, (4) drag, and (5) pressure at a far-field flow speed of 2 m/s.

Three-dimensional right whale model

Nousek-McGregor (2010) modified a primitive three-dimensional NARW model in Blender 2.49 (Blender Foundation, 2010) based on geometric measurements of NARW from necropsy measurements and aerial photogrammetry. The static, morphologically accurate 10 m (length over all, LoA) NARW model was used for CFD simulations. The NARW model was displayed at its neutral gliding position with flippers' midline perpendicular to the longitudinal axis of the animal and the dihedral angle of both flippers was 45 degrees below the horizontal platform. The fluke is displayed in the simulated neutral orientation in (Figure 1a).

Hydrodynamic parameters

Far-field flow speed

Hydrodynamic forces such as shear stress and drag are dependent on the relative speed between the surrounding fluid and the submerged object. To estimate the baseline forces on the NARW model, swimming speeds from 0.125 m/s to 8 m/s were simulated within the CFD study and the NARW model was assumed to remain static (non-articulating). The NARW model was centered at the frontal plane of the computational domain and placed somewhat closer to the front because adequate distance is needed for turbulent flow trailing behind the animal to become stable.

Reynolds number

The dimensionless speed is given by the Reynolds number, Re , which expresses the ratio of inertial forces to viscous forces and is defined by

$$Re = \frac{UL}{\nu} \quad (1)$$

where U , L , and ν are, respectively, far-field flow speed, body length, and fluid kinematic viscosity. Reynolds number further characterizes the flow regimes: at a lower Reynolds number, the flow is laminar whereas the flow becomes turbulent as the Reynolds number exceeds a critical value (Vogel 1994). For the

present work, we used the overall length of the animal, 10 m, as the length scale in calculating the Reynolds number.

Drag coefficient

For reporting the dimensionless drag, we use the drag coefficient,

$$C_D = \frac{D}{\frac{\rho}{2} U^2 A} \quad (2)$$

where D , ρ , and A are the drag force, fluid density, and drag area, respectively. For the drag area (discussed further in the Results section), we use the whale's exterior surface area; 48.42 m² for the NARW model used in this study.

Numerical model

Our CFD simulations on the representative 10 m NARW model were conducted using the SolidWorks Flow Simulation 2019 software package. The simulations were performed in a computational domain with 14 m (wide) x 14 m (high) x 27 m (long) dimensions (Figure 1b). This computational domain was selected following a detailed domain size and mesh density convergence study. The simulations employed transport equations for turbulent kinetic energy and turbulent energy dissipation rate (k - ε model). The default wall roughness and turbulence parameters were used as these gave reasonable results in our previous work (Weber *et al.* 2011). The flow solver used a single system of equations to simulate laminar and turbulent flow with transition between these flow regimes enabled. Laminar to turbulent transition is handled via the method of modified wall functions using Van Driest's profile instead of a logarithmic profile. Integral boundary layer theory is used if the local mesh size is smaller than the local boundary layer. Additional details of the simulation methods are available in the SolidWorks Flow Simulation technical documentation (Dassault Systemes SolidWorks Corporation, Waltham, MA). As inconsistent results were obtained with the automatic mesh refinement feature of the software in our previous work (Weber *et al.* 2011), we manually

specified the mesh geometry following a detail mesh convergence study with finite volume cells concentrating near the NARW model surface. For the full-domain simulations, we used a total of 11,517,423 finite volume cells. We ran 12 parallel flow speed simulations with the average solution time of approximately 4 hours per simulation on an 80-processor workstation with 256 GB of RAM. When we undertook CFD simulations on the NARW model in its half-domain, we found discontinuous flow regimes on its midline (Figure 2), this issue was resolved when we ran full-domain simulations instead. Therefore, we believe that the flow regime results near the midplane are artificial and result from a numerical interaction between the symmetry plane and the turbulence model. Other results, such as drag, shear stress, and pressure distribution, were not significantly affected by the symmetry plane – turbulence model interaction.

Results

We examined Reynolds numbers and drag coefficients for each tested flow speed and focused on hydrodynamic parameters measured at a far-field flow speed of 2 m/s. Particle pathlines simulated at a speed of 2 m/s around the left pectoral fin (Figure 3a) and the left fluke (Figure 3b) of our NARW model show blue recirculating regions that indicate partial stall for the pectoral flipper and tip vortices that occur at the tip of both the pectoral fin and the fluke (Figure 3, red arrows) indicating lift generation by these surfaces.

Fluid velocity and Reynolds number

As shown in Figure 4, we found that the drag force vs. Reynolds number fit to a quadratic polynomial model (Figure 4a, squares; $R^2=1$) whereas the drag coefficient was weakly dependent on Reynolds number (Figure 4a and 4b, dots). Fluid velocity on the medial plane of the NARW model at a far-field flow speed of 2 m/s is shown in Figure 5. Higher fluid velocities on the animal appeared at mid-body regions (approximately 0.3 to 0.6 LoA) of the NARW, where the cross-sectional area of the animal was the greatest, and above its

blowholes (Figure 5, orange-red colors). Lower fluid velocities appeared at regions before the rostrum and within the thin layer of water attaching to the NARW (i.e., the boundary layer; Figure 5, cyan-green colors). Lowest flow velocity was found at the tip of the rostrum at 0 m/s (Figure 5, blue color).

Boundary layer thickness and type

The boundary layer attaching to the NARW can be distinguished from surroundings by the visualized flow speeds over the animal as shown in Figure 5: overall thin boundary layer in regions of thickening animal cross-section (from the rostrum to approximately 0.6 LoA) and thickening boundary layer in regions of diminishing cross-section (from approximately 0.6 LoA to fluke tips). The thickest boundary layer, over 23cm, was found at the lateral sides of the peduncle, before the insertion point of the fluke (Figure 6a, regions in red) whereas the boundary layer over the outer parts of the fluke had a thickness less than 1.7cm (Figure 6a, regions in blue on the flukes). As can be seen from Figure 6b, the flow was laminar from the tip of the rostrum to approximately 0.6 LoA (Figure 6b, regions in blue) and was fully turbulent from approximately 0.8 LoA to the fluke notch (Figure 6b, regions in red). Furthermore, laminar flow occurred on the surface of the fluke outside of the body wake region (Figure 6b, regions in blue on the flukes).

Shear stress, drag, and pressure

In order to make some computations less expensive, the distributions of shear stress, form drag, and pressure on the NARW model were simulated in half domain as these quantities were unaffected by any symmetry plane – turbulence model interaction and are shown in Figure 7 and 8. The shear stress (Figure 7a) and its z component, the form drag (Figure 7b), were in opposite directions therefore the shading of the form drag was inverted (i.e., warmer colors indicate lower absolute values of drag force). The shear stress and the form drag were higher in regions facing forward on the head, which correspond to the blunt shape and irregular outlines of the head. A few body parts also experienced higher form drag forces, e.g., the leading edge of the appendages (i.e., flippers and fluke). We found higher drag on the surface of the flippers and fluke close to the trailing edge.

The gradient of pressure force on the NARW model is presented in Figure 8. The highest pressure occurred at the tip of the rostrum, which is the stagnation point of the NARW, and the leading edge of the appendages (Figure 8, red color). Pressure in the head region and between approximately 0.6 LoA to the fluke notch was higher than in the mid-body regions (approximately 0.4 to 0.6 LoA), and the observed pressure distribution was comparable to the differences in fluid velocity shown in Figure 5. This phenomenon follows Bernoulli's principle (outside of the boundary layer): lower pressure is accompanied by higher flow speed and the fluid velocity is zero at the stagnation point.

Discussion

Previous studies have shown the necessity and some attempts at evaluating drag on free-swimming and entangled NARWs to understand the effects of entanglement in fishing gear on this species (van der Hoop *et al.* 2016, van der Hoop *et al.* 2017c, van der Hoop *et al.* 2014, van der Hoop *et al.* 2017a, Knowlton *et al.* 2016, Knowlton *et al.* 2012, Cassoff *et al.* 2011, Moore & van der Hoop 2012). However, drag predictions under various circumstances are fragmentary. Hence, the initial objective of this study was to obtain the baseline drag on a NARW across a range of swimming speeds via a computational approach.

Body length, surface area, and enclosed volume for Re and C_D

The similarity variables used for reporting dimensionless speed and drag, namely the Reynolds number and drag coefficient, require the input of length and area. For calculation of the Reynolds number, we use the whale's total overall length. For calculating the drag coefficient, the choice of drag area depends on the general drag-producing body and the dominant drag mechanics; for example, friction drag or pressure drag. Because we placed the NARW model at the central region of the cross section of the computational domain (i.e., the animal was not at or close to the surface as shown in Figure 1b), wave drag was not considered in this paper (Fish 2000). The drag area, A , is defined as

$$A \approx \frac{D}{q} \quad (3)$$

where D is the drag force and the dynamic pressure, q , is defined by

$$q = \frac{\rho}{2} U^2. \quad (4)$$

In equation (4), ρ is the fluid density and U is the far-field flow speed. In the absence of an informed choice of the appropriate area to use for calculation of the drag coefficient, equation (2), the drag area given by equation (3) may be used (Hoerner 1965). Friction drag arises from fluid shearing force in a laminar or turbulent (or both) boundary layer and is typically the dominant drag mechanism for streamlined bodies in the absence of large regions of flow separation and in the absence of wave drag.

Hydrodynamic performance of the NARW

Our model simulated local flow speeds and hydrodynamic forces on the NARW model (Figure 5, 7 and 8) and the gradient of such forces can be distinguished in regard to the contours of the model, especially in its head and post-nuchal regions. The results presented here may serve as a reference for future research that seeks for an ideal location to attach tags to NARWs. In addition, we found the frontal areas that face incoming flow endure higher drag, approximately two times the drag on adjacent areas. This finding is especially valuable when one investigates animals that are in poor body condition. Currently, researchers at the New England Aquarium (Boston, MA) have a protocol to assess NARW health. The body condition score is determined by the amount of fat in an individual's neck area (Pettis *et al.* 2004). Once an animal becomes emaciated, its body shape changes and usually concavities in the neck regions will be observed. Based on our model, we hypothesize that such concavities may (1) make an animal suffer higher drag because the frontal areas are enlarged and (2) destroy the boundary layer attaching to the animal. Under selective pressure, the ancestors of modern cetaceans developed streamlined body shapes and transformed limbs to successfully return to aquatic environments (Fish 1993a, Lighthill 1969, Lighthill 1970).

Cetaceans, along with many other aquatic animals, have specialized morphology that delays separation of boundary layer and reduce drag while swimming. Therefore, shifting from healthy body condition to less-streamlined body shape makes flow separation on the animal occur earlier and the laminar flow will transit to turbulent flow earlier and ultimately cause higher drag. Emaciation indicates that the animal cannot intake enough food to support its basal metabolism and locomotive cost while non-ideal body shape makes this situation worse. For those NARWs that become emaciated due to entanglement in fishing gear, they may therefore still experience higher drag after they are freed and need longer time to recover. If it is a reproductive female, its birth interval could be extended in order to replenish fat after a combination of reproduction and entanglement. Previous study show that recovering from less-streamlined body shape to optimal body condition may take approximately a year to be visually observed for minor-to-moderate entangled individuals and resting females (Pettis *et al.* 2017). Therefore, we recommend that potential greater energy expenditure associated with transformed body shape should serve as an additional factor when conducting animal and population health assessments.

Whale drag predictions

By referring to the non-dimensional drag coefficient of a submerged object, drag forces are comparable between objects of different shapes under various flow conditions as long as the dimensionless similitude parameters match. For that reason, measurements of drag coefficient from current and previous studies across cetacean taxa are plotted as a function of Reynolds number in Figure 9 in order to compare drag coefficients across different body shapes, lengths, and swimming speeds (Bose & Lien 1989, Nousek-McGregor 2010, van der Hoop *et al.* 2014, Miller *et al.* 2004, Lang & Daybell 1963, Fish 1998). The values of drag coefficients from the literature are shown in Table 1. Nousek-McGregor (2010) undertook CFD simulations on a three-dimensional NARW model and calculated drag with a hydrodynamic model and data collected from NARWs in their habitats. van der Hoop *et al.* (2014) also calculated drag with a hydrodynamic model and data recorded by animal-borne tags attached to a NARW. Lang and Daybell (1963) estimated

drag with a hydrodynamic model and data collected from the literature, a blue whale (*B. musculus*), and from video footage of a captive Pacific white side dolphin (*L. obliquidens*). Miller *et al.* (2004) calculated drag on sperm whales (*P. macrocephalus*) with a hydrodynamic model and data recorded by animal-borne tags. Fish (1998) video-recorded captive cetaceans, including orcas (*O. orca*), false killer whales (*P. crassidens*), belugas (*D. leucas*), and bottlenose dolphins (*T. truncatus*), and estimated drag based on decelerations of the video-recorded animals. Drag coefficients of a fin whale (*B. physalus*) fluke calculated by Bose and Lien (1989) are included for comparing research methods. As shown in Figure 9, under similarity conditions, which are represented by Reynolds number here, these animals are affected by drag at different levels and we found that our drag estimation for NARW was higher than predicted by previous studies for other large whale species.

While there is no need to know exactly the component values of each component of drag coefficients and Reynolds numbers for each species to undertake such comparisons (Vogel 1994), one must acknowledge that (1) every drag coefficient and Reynolds number is calculated under a particular condition, regardless of which parameter has changed in the course of measurements and (2) both experimental (e.g., video footage and tagging) and numerical (e.g., CFD simulation) approaches simplify the calculation. Possible explanations for such diverse results may be differences in the morphology of the animals, their swimming speeds and capabilities, and various methods used to calculate drag. For instance, when cruising at similar speeds, slender body shapes of rorquals suggest that they encounter lower drag and have higher swimming efficiency than NARWs, sperm whales, and belugas (Fish 1998, Woodward *et al.* 2006, Goldbogen *et al.* 2006), whereas the latter species have developed corresponding morphological or behavioral specializations to overcome inefficiency due to their body form. Higher swimming speeds during foraging observed in *Delphinidae* such as orcas and bottlenose dolphins force them to endure higher drag since drag increases with the square of speed (Fish 1998, Vogel 1994). Lastly, advanced computer technology enhances the resolution of three-dimensional NARW models and CFD flow solvers, and therefore provides

more precise drag estimations. The capabilities of modern computers and filming equipment are also crucial for analyzing video recordings of captive animals.

Limitations of drag estimation

It is important to bear in mind the simplified calculations utilized by both hydrodynamic and CFD models. For example, in the cases of estimating drag from animal-borne tags and video recordings (i.e., *in situ* measurements), the outcome forces comprise not only the small-scale flow circulating on the animal but also currents and waves (e.g., wave drag) if the animal is close enough to the surface (Vogel 1994). In other words, the hydrodynamic models have taken the environmental impacts into account while the CFD models assume that the incoming flow is turbulence-free and neither sea surface nor sea floor is included in the calculation. However, those physical factors experienced by animals in the real world are unlikely identical in any part of the water column, which implies that the drag estimations calculated from *in situ* data are correct under specific conditions but not other conditions. On the other hand, even though the discrete cells in the three-dimensional animal model and flow simulated in high resolution calculations provide more accurate drag estimations, CFD simulations assume the animal is a rigid body without flexibility and maneuverability. By doing so, CFD models generate a best-estimate of the baseline drag on the animal but overlook the impacts of trailing vortices induced by animal locomotion, fluke pitching and undulating of the whole body for example, which also known as the induced drag (Lighthill 1969, Hall & Hall 1996, Hall & Howle 2005). In addition, differences between skin texture or roughness of the three-dimensional model and real tissue suggest bias toward calculations of friction force (i.e., the skin is not completely smooth on real animals, particularly the rough callosities on the heads of NARWs). Moreover, when calculating drag coefficient, most models simplify the outline of an animal by applying the equation derived for a flat plate or body of revolution (see above discussions on animal length, surface area, and enclosed volume), although the shape of cetaceans is to some extent between a flat plate and a blunt body, which is varied among species (Fish 2002).

Conclusion

This is the first comprehensive study of drag and other hydrodynamic characteristics of NARWs through a CFD approach. Our results show that drag on NARWs is higher than previous estimates on this species and measurements of other large whales. Since NARWs are frequently observed being entangled in fishing gear and consequently some individuals suffer from emaciation, investigations on potential increased energetic costs due to imperfect body shapes are required for animal health assessments. Given the capability of CFD models to provide detailed force distributions on a whale model as shown in the present study, it is practicable that this method can be applied to estimating hydrodynamic forces on animals with various body shapes.

Acknowledgements

Dan Maas (Maas Digital) greatly improved the 3D right whale model and comments from Michael Moore (WHOI) and Bill McLellan (University of North Carolina - Wilmington) were invaluable in creating a morphologically accurate model. Wayne Perryman and Paula Olsen at SWFSC provided assistance with obtaining accurate 2D measurements of right whales through their aerial photogrammetry.

References

- Bose, N. and J. Lien. 1989. Propulsion of a Fin Whale (*Balaenoptera-Physalus*): Why the Fin Whale Is a Fast Swimmer. *Proceedings of the Royal Society Series B-Biological Sciences* 237:175-200.
- Cassoff, R. M., K. M. Moore, W. A. McLellan, S. G. Barco, D. S. Rotstein and M. J. Moore. 2011. Lethal entanglement in baleen whales. *Diseases of Aquatic Organisms* 96:175-185.
- Drucker, E. G. and G. V. Lauder. 2002. Experimental Hydrodynamics of Fish Locomotion: Functional Insights from Wake Visualization. *Integrative and Comparative Biology* 42:243-257.
- Fish, F. E. 1993a. Influence of Hydrodynamic: Design and Propulsive Mode on Mammalian Swimming Energetics. *Australian Journal of Zoology* 42:79-101.
- Fish, F. E. 1993b. Power Output and Propulsive Efficiency of Swimming Bottle-Nosed Dolphins (*Tursiops-Truncatus*). *Journal of Experimental Biology* 185:179-193.
- Fish, F. E. 1998. Comparative kinematics and hydrodynamics of odontocete cetaceans: Morphological and ecological correlates with swimming performance. *Journal of Experimental Biology* 201:2867-2877.

- Fish, F. E. 2000. Biomechanics and energetics in aquatic and semiaquatic mammals: Platypus to whale. *Physiological and Biochemical Zoology* 73:683-698.
- Fish, F. E. 2002. Balancing requirements for stability and maneuverability in cetaceans. Pages 85-93 *Integrative and Comparative Biology*. Chicago, Illinois.
- Goldbogen, J. A., J. Calambokidis, R. E. Shadwick, E. M. Oleson, M. A. McDonald and J. A. Hildebrand. 2006. Kinematics of foraging dives and lunge-feeding in fin whales. *Journal of Experimental Biology* 209:1231-1244.
- Goldbogen, J. A., N. D. Pyenson and R. E. Shadwick. 2007. Big gulps require high drag for fin whale lunge feeding. *Marine Ecology Progress Series* 349:289-301.
- Hall, K. C. and S. R. Hall. 1996. Minimum induced power requirements for flapping flight. *Journal of Fluid Mechanics* 323:285-315.
- Hall, K. C. and L. E. Howle. 2005. The Mechanics of Flapping Flight: Final report on research funded by NASA Langley Research Center (NASA Grant NAG 1-01062). pp.
- Hoerner, S. F. 1965. Fluid-dynamic drag: practical information on aerodynamic drag and hydrodynamic resistance. Hoerner Fluid Dynamics, Midland Park, N.J.
- Howle, L. E., S. D. Kraus, T. B. Werner and D. P. Nowacek. 2018. Simulation of the entanglement of a North Atlantic (*Eubalaena glacialis*) with fixed fishing gear. *Marine Mammal Science* 35:760-778.
- Knowlton, A. R., P. K. Hamilton, M. K. Marx, H. M. Pettis and S. D. Kraus. 2012. Monitoring North Atlantic right whale *Eubalaena glacialis* entanglement rates: a 30 yr retrospective. *Marine Ecology Progress Series* 466:293-302.
- Knowlton, A. R., J. Robbins, S. Landry, H. A. McKenna, S. D. Kraus and T. B. Werner. 2016. Effects of fishing rope strength on the severity of large whale entanglements. *Conservation Biology* 30:318-328.
- Kraus, S. D., M. W. Brown, H. Caswell, C. W. Clark, M. Fujiwara, P. K. Hamilton, R. D. Kenney, A. R. Knowlton, S. Landry, C. A. Mayo, W. A. McLellan, M. J. Moore, D. P. Nowacek, D. A. Pabst, A. J. Read and R. M. Rolland. 2005. Ecology. North Atlantic right whales in crisis. *Science* 309:561-562.
- Kraus, S. D., R. D. Kenney, C. A. Mayo, W. A. McLellan, M. J. Moore and D. P. Nowacek. 2016. Recent Scientific Publications Cast Doubt on North Atlantic Right Whale Future. *Frontiers in Marine Science* 3:137.
- Lang, T. G. and D. A. Daybell. 1963. Porpoise performance tests in a seawater tank. China Lake, California.
- Lighthill, M. J. 1969. Hydromechanics of Aquatic Animal Propulsion. *Annual Review of Fluid Mechanics* 1:413-446.
- Lighthill, M. J. 1970. Aquatic Animal Propulsion of High Hydromechanical Efficiency. *Journal of Fluid Mechanics* 44:265-301.
- Miller, P. J. O., M. P. Johnson, P. L. Tyack and E. A. Terray. 2004. Swimming gaits, passive drag and buoyancy of diving sperm whales *Physeter macrocephalus*. *Journal of Experimental Biology* 207:1953-1967.
- Moore, M., M. Walsh, J. Bailey, D. Brunson, F. Gulland, S. Landry, D. Mattila, C. Mayo, C. Slay, J. Smith and T. Rowles. 2010. Sedation at Sea of Entangled North Atlantic Right Whales (*Eubalaena glacialis*) to Enhance Disentanglement. *Plos One* 5:e9597.
- Moore, M. J. 2014. How we all kill whales. *ICES Journal of Marine Science* 71:760-763.
- Moore, M. J. and J. M. Van Der Hoop. 2012. The Painful Side of Trap and Fixed Net Fisheries: Chronic Entanglement of Large Whales. *Journal of Marine Biology* 2012.
- Nousek-Mcgregor, A. E. 2010. The cost of locomotion in North Atlantic right whales (*Eubalaena glacialis*). Doctoral Thesis, Duke University.

- Pettis, H. M., R. M. I. Pace and P. K. Hamilton. 2018. North Atlantic Right Whale Consortium 2018 Annual Report Card. Report to the North Atlantic Right Whale Consortium. 17 pp.
- Pettis, H. M., R. M. Rolland, P. K. Hamilton, S. Brault, A. R. Knowlton and S. D. Kraus. 2004. Visual health assessment of North Atlantic right whales (*Eubalaena glacialis*) using photographs. *Canadian Journal of Zoology-Revue Canadienne De Zoologie* 82:8-19.
- Pettis, H. M., R. M. Rolland, P. K. Hamilton, A. R. Knowlton, E. A. Burgess and S. D. Kraus. 2017. Body condition changes arising from natural factors and fishing gear entanglements in North Atlantic right whales *Eubalaena glacialis*. *Endangered Species Research* 32:237-249.
- Sharp, S. M., W. A. Mclellan, D. S. Rotstein, A. M. Costidis, S. G. Barco, K. Durham, T. D. Pitchford, K. A. Jackson, P. Y. Daoust, T. Wimmer, E. L. Couture, L. Bourque, T. Frasier, B. Frasier, D. Fauquier, T. K. Rowles, P. K. Hamilton, H. Pettis and M. J. Moore. 2019. Gross and histopathologic diagnoses from North Atlantic right whale *Eubalaena glacialis* mortalities between 2003 and 2018. *Diseases of Aquatic Organisms* 135:1-31.
- Shorter, K. A., M. M. Murray, M. Johnson, M. Moore and L. E. Howle. 2014. Drag of suction cup tags on swimming animals: Modeling and measurement. *Marine Mammal Science* 30:726-746.
- Van Der Hoop, J., P. Corkeron, A. Henry, A. Knowlton and M. Moore. 2017a. Predicting lethal entanglements as a consequence of drag from fishing gear. *Marine Pollution Bulletin* 115:91-104.
- Van Der Hoop, J., P. Corkeron and M. Moore. 2017b. Entanglement is a costly life-history stage in large whales. *Ecology and Evolution* 7:92-106.
- Van Der Hoop, J., M. Moore, A. Fahlman, A. Bocconcelli, C. George, K. Jackson, C. Miller, D. Morin, T. Pitchford, T. Rowles, J. Smith and B. Zoodsma. 2014. Behavioral impacts of disentanglement of a right whale under sedation and the energetic cost of entanglement. *Marine Mammal Science* 30:282-307.
- Van Der Hoop, J. M., P. Corkeron, J. Kenney, S. Landry, D. Morin, J. Smith and M. J. Moore. 2016. Drag from fishing gear entangling North Atlantic right whales. *Marine Mammal Science* 32:619-642.
- Van Der Hoop, J. M., D. P. Nowacek, M. J. Moore and M. S. Triantafyllou. 2017c. Swimming kinematics and efficiency of entangled North Atlantic right whales. *Endangered Species Research* 32:1-17.
- Van Der Hoop, J. M., A. S. M. Vanderlaan, T. V. N. Cole, A. G. Henry, L. Hall, B. Mase-Guthrie, T. Wimmer and M. J. Moore. 2015. Vessel Strikes to Large Whales Before and After the 2008 Ship Strike Rule. *Conservation Letters* 8:24-32.
- Vogel, S. 1994. *Life in moving fluids: the physical biology of flow*. Princeton University Press, Princeton, NJ.
- Weber, P. W., L. E. Howle, M. M. Murray and D. S. Miklosovic. 2011. Computational Evaluation of the Performance of Lifting Surfaces with Leading-Edge Protuberances. *Journal of Aircraft* 48:591-600.
- Williams, T. M. and J. L. Maresh. 2015. Exercise energetics. Pages 47-68 in M. A. Castellini and J.-A. Mellish eds. *Marine Mammal Physiology: Requisites for Ocean Living*. CRC Press, Boca Raton, FL.
- Woodward, B. L., J. P. Winn and F. E. Fish. 2006. Morphological specializations of baleen whales associated with hydrodynamic performance and ecological niche. *Journal of Morphology* 267:1284-1294.
- Zhang, D., J. M. Van Der Hoop, V. Petrov, J. Rocho-Levine, M. J. Moore and K. A. Shorter. 2019. Simulated and experimental estimates of hydrodynamic drag from bio-logging tags. *Marine Mammal Science Online*.

Table

Table 1. Drag coefficients across taxa from current and previous studies.

Species	LoA ^{&} (m)	Re ($\times 10^7$)	C _d ($\times 10^{-3}$)	Model	Reference
<i>Eubalaena glacialis</i>	10	1.24-7.96	7.7-5.3	CFD	Current study
<i>Eubalaena glacialis</i>	15	0.771*	12	CFD	Nousek-McGregor (2010)
<i>Eubalaena glacialis</i>	10-13	0.90-1.30*	5.9-3.6	SHM [§]	Nousek-McGregor (2010)
<i>Eubalaena glacialis</i>	9.45	0.73-2.81*	3.7-2.9	SHM	van der Hoop <i>et al.</i> (2014)
<i>Balaenoptera musculus</i>	21.95	17-52	2.3-1.9	SHM	Lang and Daybell (1963)
<i>Balaenoptera physalus</i>	14.5	4.28-12.9	2.64-2.26 [†]	SHM	Bose and Lien (1989)
<i>Physeter macrocephalus</i>	10.0-13.4	1.92	3.06	SHM	Miller <i>et al.</i> (2004)
<i>Orcinus orca</i>	3.81-5.57	0.909-3.65	15.4-2.6	SHM	Fish (1998)
<i>Pseudorca crassidens</i>	3.55-3.99	0.535-2.71	10.8-4.7	SHM	Fish (1998)
<i>Delphinapterus leucas</i>	3.25-4.12	0.500-1.30	26.5-12.7	SHM	Fish (1998)
<i>Tursiops truncatus</i>	2.51-2.70	0.245-1.48	27-7.7	SHM	Fish (1998)
<i>Lagenorhynchus obliquidens</i>	2.04	0.61-1.83	3.67-3.08 [‡]	SHM	Lang and Daybell (1963)

[&]length of the animal
[§]simplified hydrodynamic model
^{*}Re values were calculated from swimming speed and animal length provided in the article while using kinematic viscosity for seawater = $1 \times 10^{-6} \text{ m}^2/\text{s}$
[†]drag on the fluke
[‡]drag on the body (appendages were excluded from calculation)

Figures

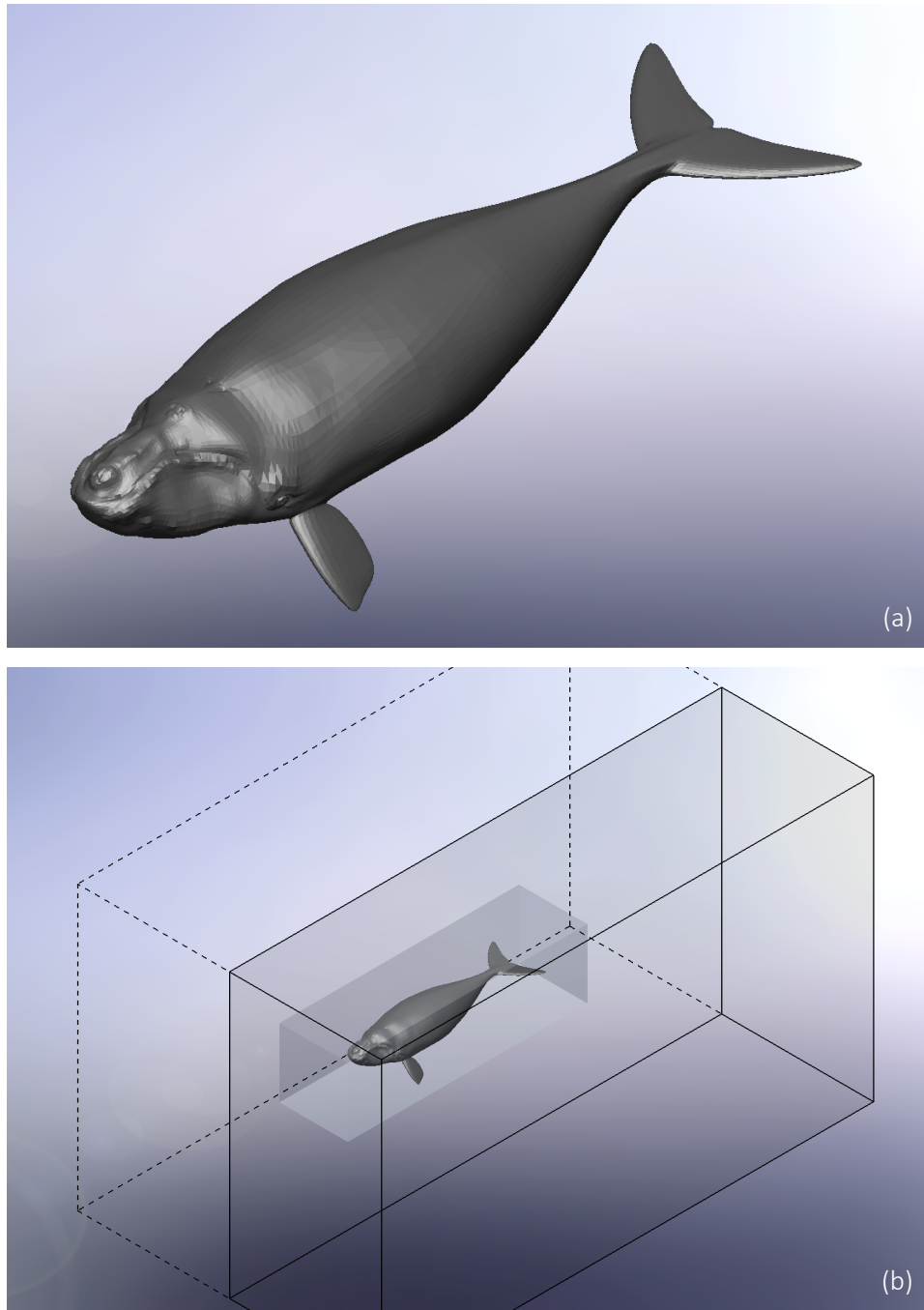


Figure 1. The three-dimensional NARW model. Note that the model (a) is displayed in its neutral gliding position in the computational domain (b) with flippers' midline perpendicular to the longitudinal axis of the animal and the dihedral angle of both flippers was 45 degrees below horizontal platform. The fluke was displayed horizontally.

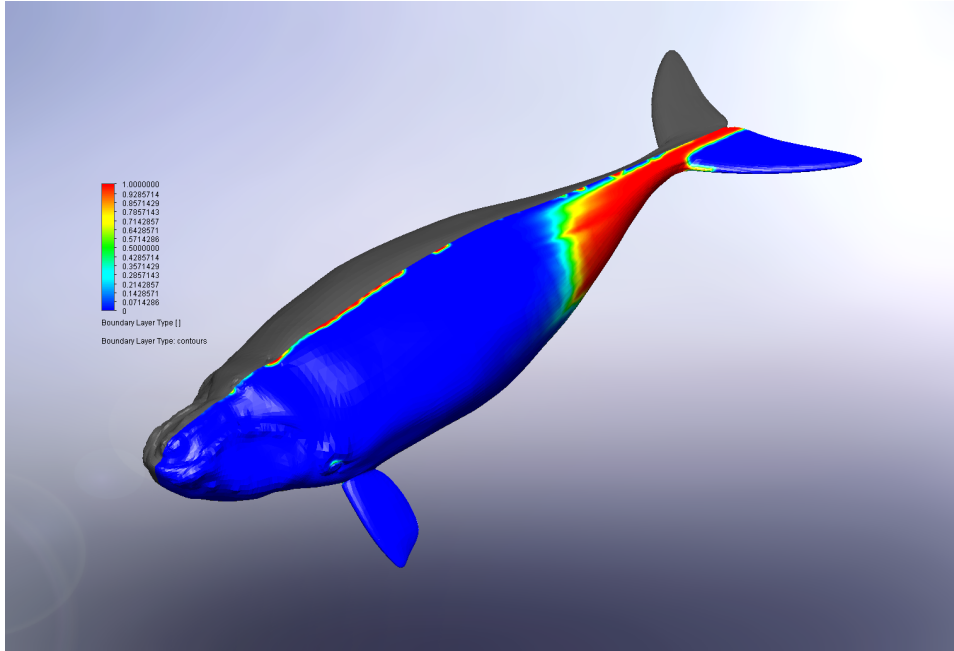


Figure 2. Boundary layer type simulated in half domain. Blue shows laminar flow while red shows turbulent flow. Intermediate colors indicate transitional flow. Turbulent flow anomalies are found at the midline of the NARW model when simulating in half-domain. This phenomenon is eliminated if the full domain model is used.

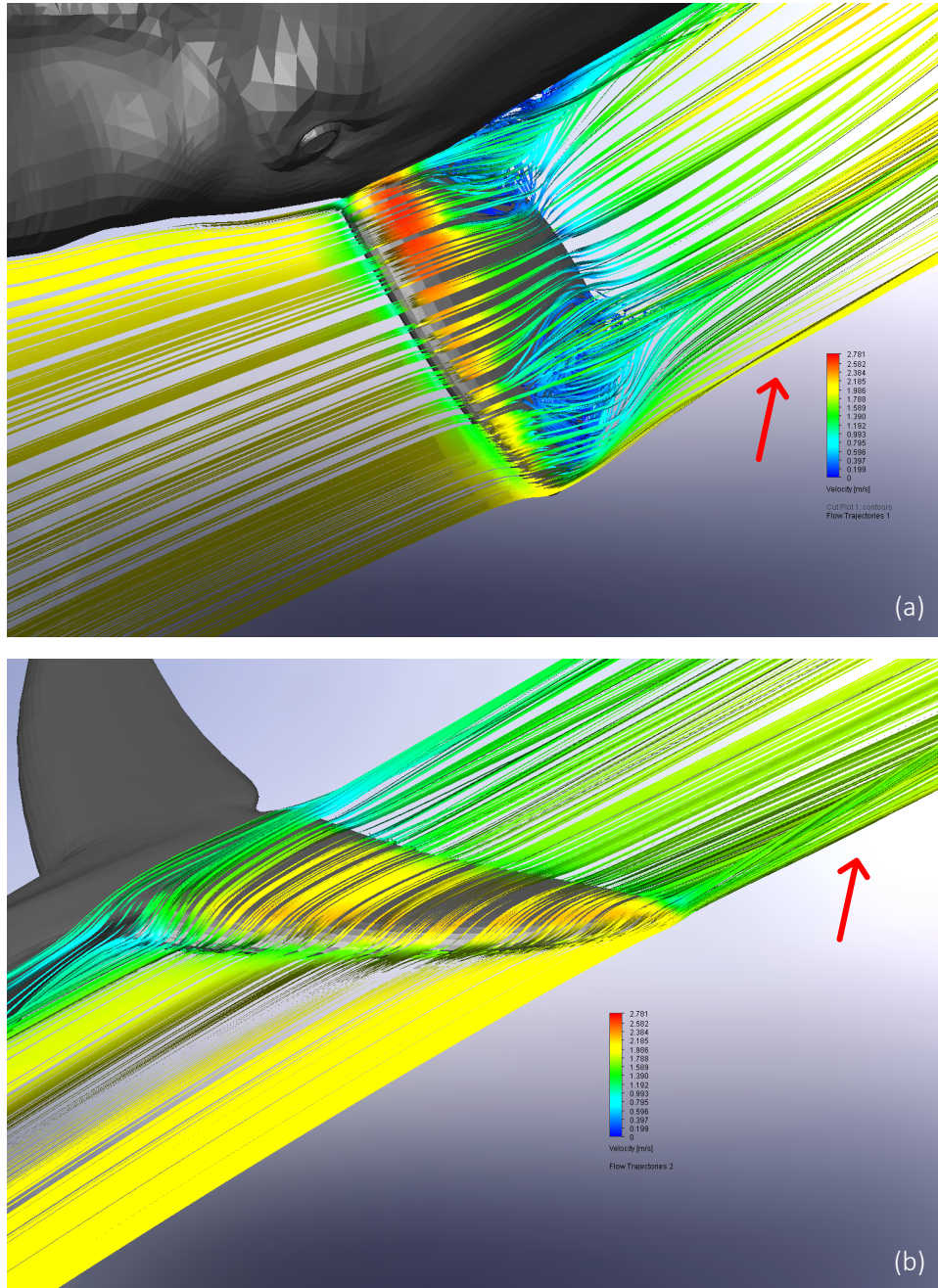


Figure 3. Particle pathlines on the left pectoral fin (a) and the left fluke (b) of the NARW model (far-field flow speed = 2 m/s). Warmer colors illustrate higher local flow speeds while cooler colors express lower speeds around the NARW. The blue recirculating regions on the left pectoral fin indicate partial stall. Tip vortices occurred at the tip of both the pectoral fin and the fluke (red arrows).

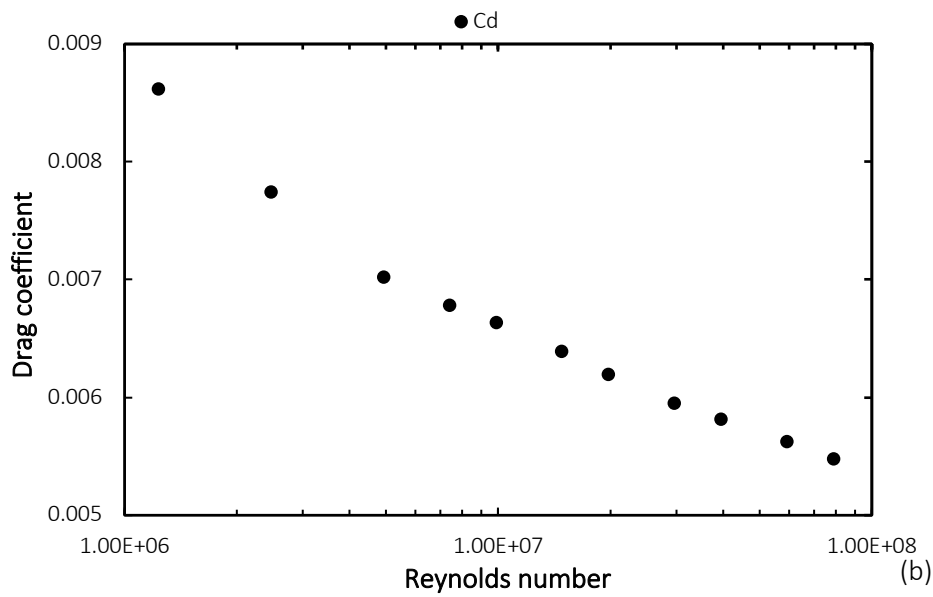
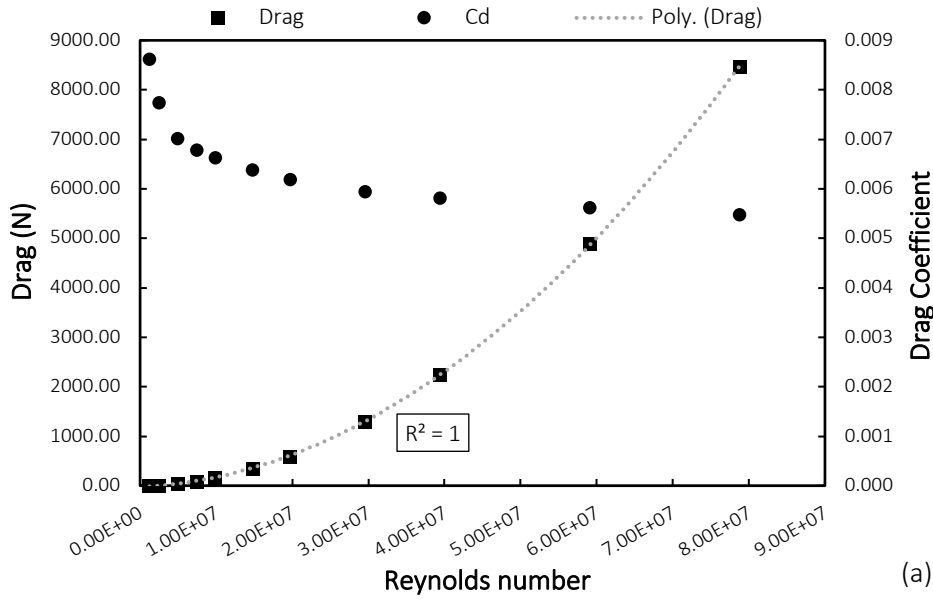


Figure 4. Drag (squares) and drag coefficient (dots) as a function of Reynolds number. Drag force and Reynolds number fit to a quadratic polynomial model (a) whereas drag coefficient is weakly dependent on Reynolds number (a, b).

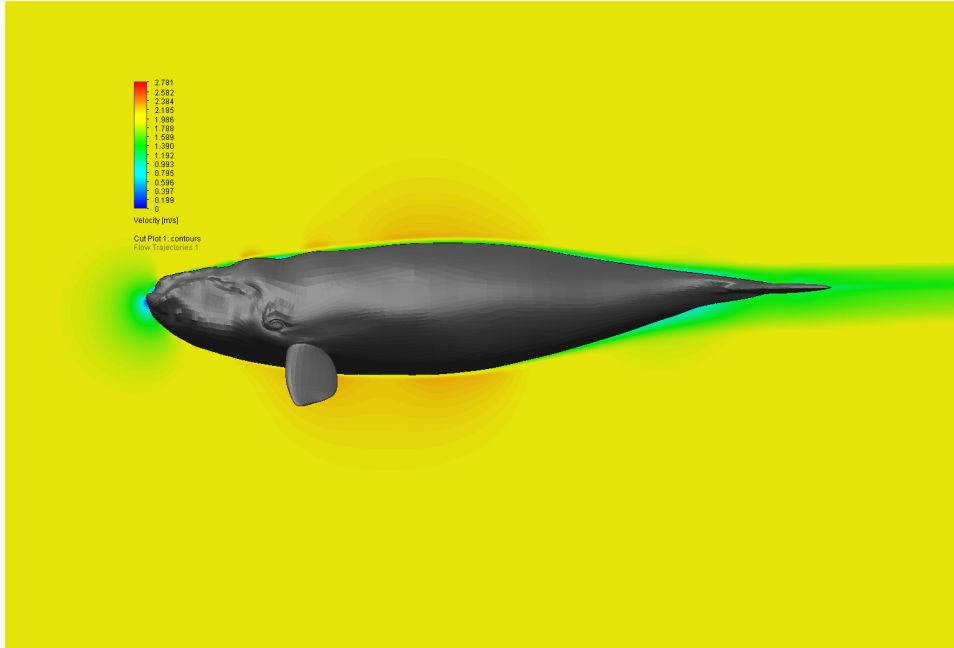


Figure 5. Fluid velocity on the medial plane of the NARW model at a nominal speed of 2 m/s. Higher fluid velocities (orange-red colors) appeared at mid-body regions (approximately 0.3 to 0.6 LoA) of the NARW, where the cross-section area of the animal is the greatest, and above its blowholes. Lower fluid velocities (cyan-green colors) appeared at regions before the rostrum and within a thin layer of water attaching to the surface of the NARW (i.e., boundary layer). Lowest fluid velocity (blue color) was found at the tip of the rostrum (stagnation point) at a flow speed of 0 m/s.

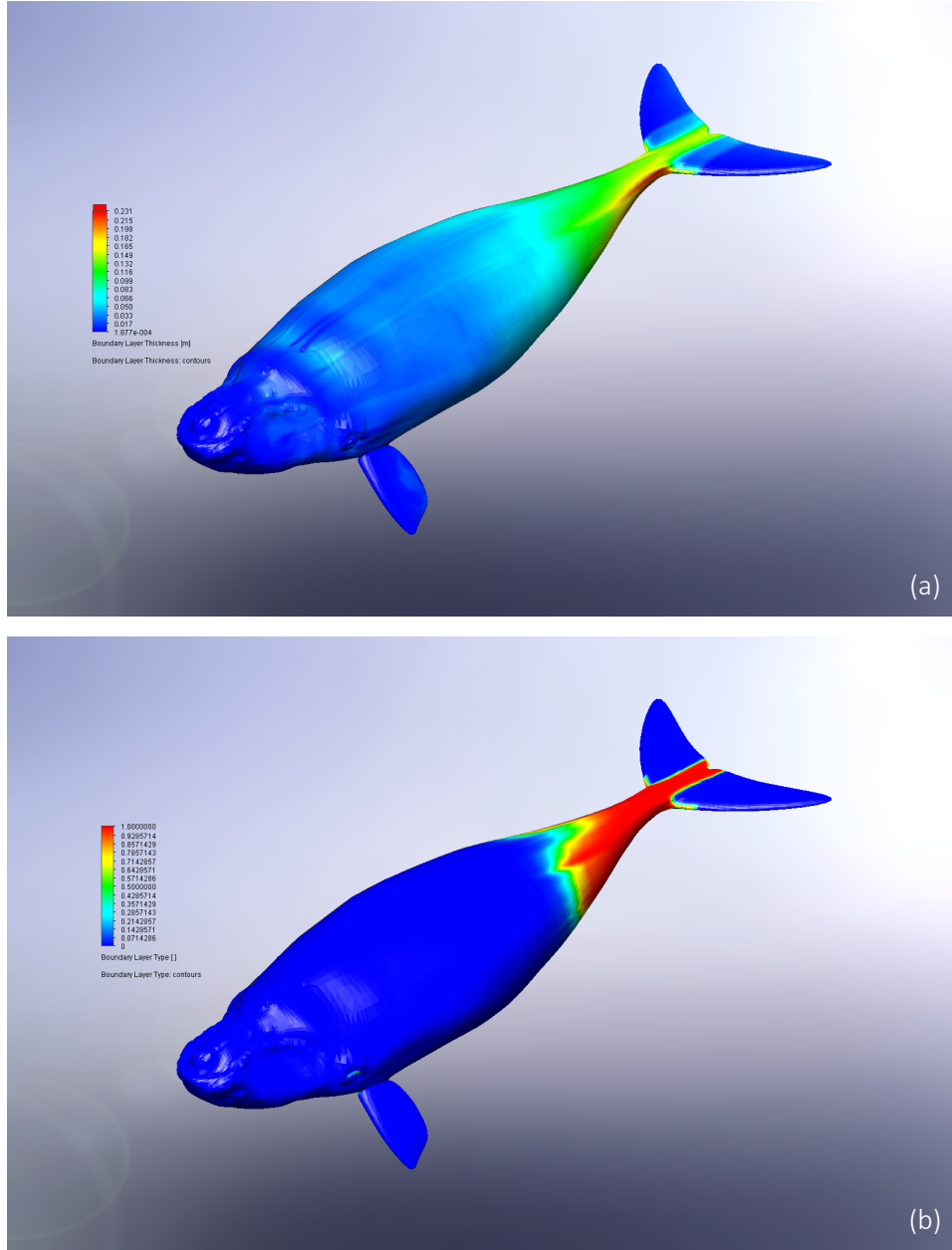


Figure 6. Boundary layer thickness (a) and type (b). Overall thin boundary layer (cooler colors) in regions of thickening animal cross-section and thickening boundary layer (warmer colors) in regions of diminishing cross-section (a). The thickest boundary layer was found at the lateral sides of the peduncle whereas the boundary layer over the outer part of the flukes was the thinnest. Flow is laminar (blue color) from the rostrum to approximately 0.6 LoA and is fully turbulent from approximately 0.8 LoA to the fluke notch (red color). Furthermore, laminar flow occurred on the surface of the flukes outside of the body wake region (b).

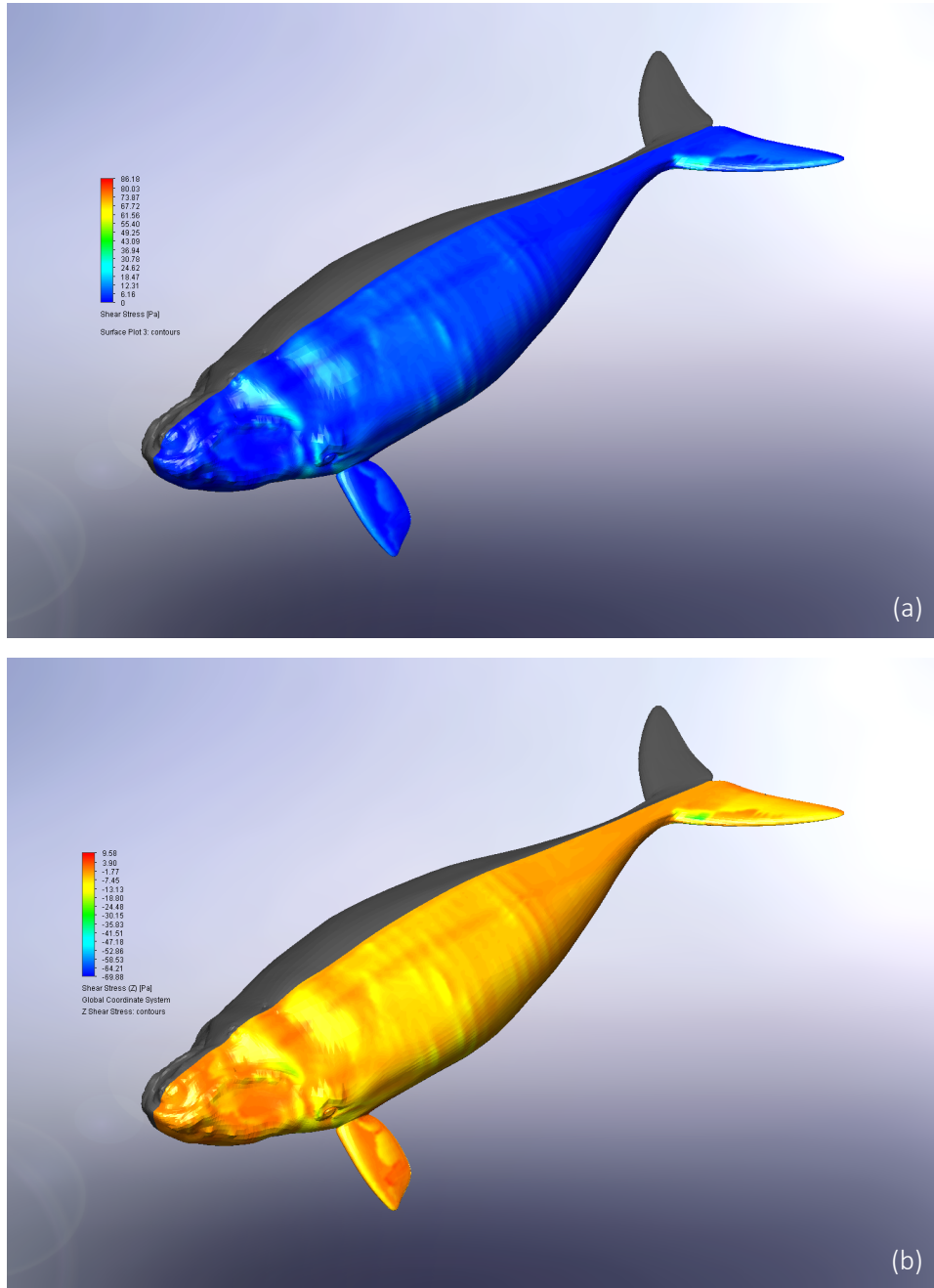


Figure 7. Shear stress (a) and form drag (b) on the NARW model. The form drag was in the opposite direction of the shear stress and therefore its shading was inverted (i.e., warmer colors indicate lower absolute values of drag force). The shear stress and the form drag were higher in regions faced forward on the head and the leading edge of the appendages. Drag on the surface of flippers and flukes close to the trailing edge was higher.

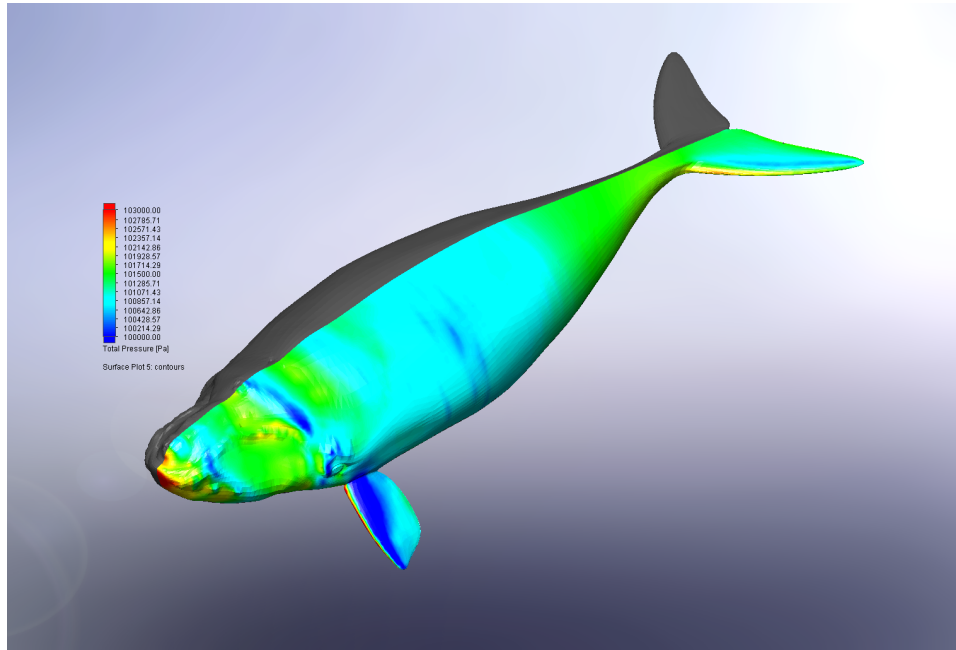


Figure 8. Pressure gradient on the NARW model. The highest pressure occurred at the tip of the rostrum and the leading edge of the appendages (red color). Pressure in head regions and approximately 0.6 LoA to the fluke notch was higher than the mid-body regions (approximately 0.4 to 0.6 LoA) of the NARW model.

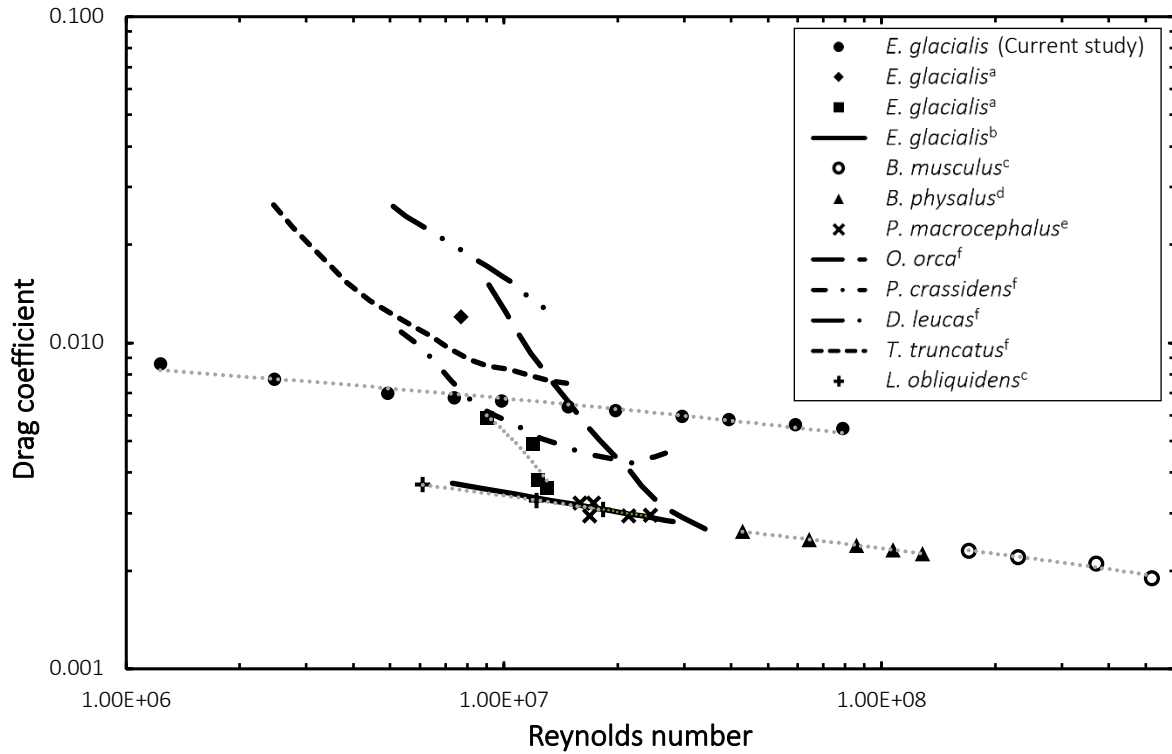


Figure 9. Drag coefficients across taxa from current and previous studies as a function of Reynolds number. Drag coefficients of large whales, including blue, fin, right, and sperm whales, are relatively smaller than orcas, false killer whales, belugas, bottlenose dolphins, and Pacific white side dolphins that have smaller body sizes under similar flow conditions, which are represented by Reynolds number. Drag coefficients from the current study of right whales (solid dots) are relatively higher among large whale species. (Refer to Table 1 for data sources.)